High sensitivity Raman imaging of the surface of casted glass plates

M. Jacquemin, P. Simon, A. Canizares, L. Hennet, C. Bessada, D. Skrelic, E. Gouillart, E. Burov

High sensitivity Raman imaging of the surface of casted glass plates

M. Jacquemin[1], P. Simon[1], A. Canizarès[1], L. Hennet[*1], C. Bessada[1], D. Skrelic[2], E. Gouillart[2], and E. Burov[2]

[1]CNRS, CEMHTI UPR3079, Univ. Orléans, F-45071 Orléans, France
[2]CNRS/Saint-Gobain Recherche, Surface du Verre et Interfaces UMR 125, 39 quai Lucien Lefranc, 93300 Aubervilliers, France

Abstract

Glass manufacturing processes are prone to induce local fluctuations of the glass properties, to which Raman spectroscopy is highly sensitive. In this work, Raman imaging is used to investigate the homogeneity of the Raman response at the surface of casted aluminosilicate glass pieces. Samples were probed at constant focus depth across 7×7 cm^2 surfaces using 500 µm spatial steps, resulting in unusually large and detailed Raman images. We show that the extent of modification of the Raman response is small across the scanned area, and that the information is mostly carried by the spatial representation of properly selected Raman parameters. Specifically, detailed macroscopic patterns correlating to the glass casting process were obtained from Raman parameters of two distinct Raman modes: the Si-O stretching mode involving Q^2 tetrahedral units, and the Si-O-Si bending vibrations envelope in the low-wavenumber range. The contrasts on the Raman images are assigned to fine local variations of fictive temperature (and hence of cooling rate) and chemistry resulting from the manufacturing process. From the evolution of these parameters across the surface of the sample, we were able to identify areas consisting of material from different stages of the casting. Structural and chemical changes originating from the manufacturing process

*Now at CNRS, ICMN UMR7374, Univ. Orléans, F-45071 Orléans, France

are therefore printed at the surface of the glass pieces, and their fingerprint revealed by Raman imaging.

Keywords: Raman imaging, glasses, glass processing

Introduction

Raman spectroscopy is a commonly used technique for the study of the local range order in glasses and melts.[1] It is appreciated for its non-destructive nature, and its versatility and relative ease of use make it particularly suitable to perform *in situ* characterizations in extreme conditions.[2–8] Modern Raman instruments are now capable of acquiring large datasets of quality spectra within reasonable timescales, allowing for spatial mapping of surfaces ranging from a few μm^2 to several cm^2 while maintaining submicronic spatial resolutions. A visualization of the probed surface can then be generated using relevant Raman spectral parameters, typically position, width or intensity of a characteristic Raman mode. The resulting image conveys information on the uniformity of the Raman response across the surface, indicating local composition, structure or phase fluctuations, for example. Coupling imaging with the high sensitivity that modern systems can achieve allows for the identification of fluctuations otherwise not visible by simple spectra comparison, offering new insights on cultural heritage materials,[9] ceramics,[10,11] glasses[12] or powdered carbon materials.[13]

Most industrial glasses are synthesized through macroscopic processes such as the industrial "float" and "fusion-draw" processes, injection molding, or at smaller scales by casting. Due to their nature, these manufacturing steps occasionally induce viscosity, density or composition gradients, and from these effects may result macroscopic variations of the glass properties that can be detrimental to the final products. Maintaining a good control over glass surface quality is of prime importance for the functionalization of glass surfaces, for example, as minor composition and density changes may result in critical alteration of the thin film stack properties. Unfortunately, although the human eye and widely used optic quality control systems are very sensitive to macroscopic variations of the glass properties, the detection of modifications induced at a smaller scale would require the use of techniques capable of achieving higher sensitivities.

In this regard, we present a Raman investigation of the surface of bulk casted glass samples of compositions close to commercially available window glass. Using spatially resolved Raman spectroscopy and imaging, we probed microscopic fluctuations over large surfaces. The homogeneity of the Raman response at the surface of the samples is assessed and implications are discussed.

Methods

Sample preparation

A series of glass samples was synthesized in the composition range 14.3-19.3 wt% (14.1-19.1 mol%) Na_2O, 11.2-16.2 wt% (12.2-17.6 mol%) CaO, 2.5-7.5 wt% (1.5-4.5 mol%) Al_2O_3, 62-67 wt% (62.9-68.2 mol%) SiO_2. 1.2 kg batches were prepared from industrial grade sand, limestone, sodium carbonate and calcined alumina, with the addition of 300 ppm of coke as fining agent. The mixtures were then melted at 1550°C for 4 hours in a Joule-heated furnace and mechanically stirred every hour. The melts were casted onto a $\sim$10×10×3 cm^3 steel shape, air-quenched and annealed for 3 hours at their respective annealing points before slowly cooling down to room temperature. This procedure consistently yielded clear, bubble-free, and visually homogeneous glass plates (Fig. 1). The chemical homogeneity of samples synthesized by this procedure was assessed by electron microprobe analysis (EMPA) in a prior study on samples of similar volume and compositions, which showed to be homogeneous with standard deviations below 0.02 wt%.[14] For the sake of simplicity, this paper will highlight results from a sample that is at the center of the composition range. This glass will be denoted C_0 and is composed as follows : 16.8 wt% (16.5 mol%) Na_2O, 13.7 wt% (14.9 mol%) CaO, 5.0 wt% (3.0 mol%) Al_2O_3, 64.5 wt% (65.5 mol%) SiO_2. Compositions of the whole sample set are provided in Table S1 (Supporting Information). Results from all characterized glasses are also provided in the Supporting Information.

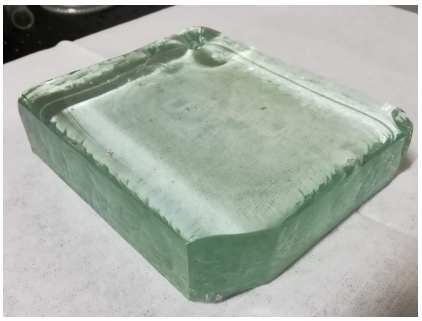

Figure 1: Example of synthesized glass plate (dimensions : 10×10×3 cm^3).

Raman mapping

Raman images were collected point-by-point on a Renishaw Invia™ Qontor® confocal microscope in backscattering geometry. The glass pieces were mounted

as-whole on custom sample holders and excited under a 514 nm laser operating at a power of 50 mW and focused through a 50× long focal objective. A surface of 7×7 cm^2 was probed by 500 µm steps in both dimensions, resulting in 141×141=19881 acquisitions per sample. The counting time was 10 s per spectrum, which allowed to record data of good quality while maintaining a reasonable experiment time of approximately 2.5 days. All measurements were recorded at room temperature. The frequency and intensity stability of the device is improved by specific temperature control of the whole spectrometer room, leading to a stability frequency better than 0.1 cm^{-1} over 24 hours.[15]

During the acquisitions, the focus was set 10 µm below the surface to minimize surface effects. In addition, we used Renishaw's LiveTrack™ focus tracking feature to accommodate the curviness of the casted samples. This feature ensures minimal variations in focus quality over the duration of the experiment. This is done by automatically adjusting the stage height during each (x,y) translation, so that the laser spot size matches a reference focus that was set 10 µm below the surface. As a result, we were able to record data while accurately following the curvature of the samples (Fig. 2).

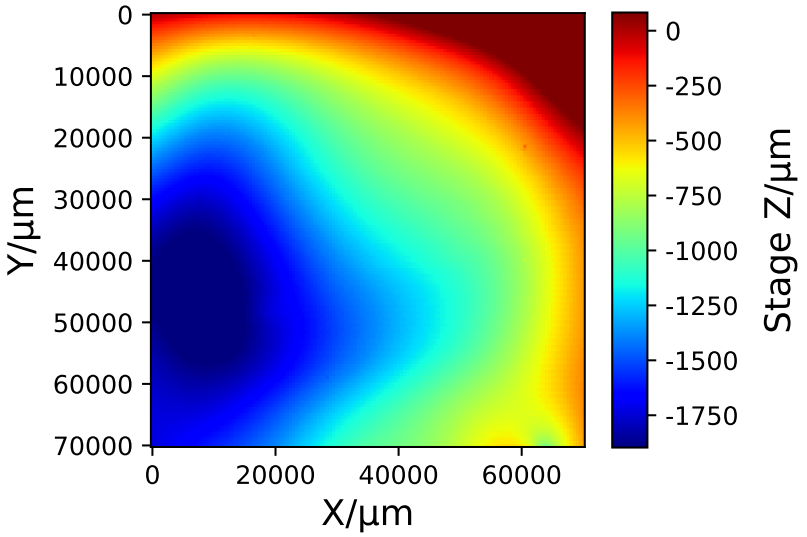

Figure 2: Variation of Raman spectrometer stage height with position on glass sample C_0. The spot size was recorded at the origin by focusing the laser 10 µm below the surface.

Data processing

All datasets were individually processed in the same manner using homemade Python routines. First, a PCA noise reduction was applied to the dataset in order to minimize the impact of the short accumulation time. The data was reconstructed using 10 components explaining >99.9% of the variance ratio. This step showed to greatly improve the quality and readability of the spectra. Background variations were corrected by subtracting the minimum value of each spectrum. Finally, all spectra were normalized to their total integrated area.

Results

The Raman response of the glass sample is first assessed by averaging the processed dataset into an average spectrum (Fig. 3). We consider this to be a good approximation of the overall response as only small variations are expected within the large dataset. This assumption is supported by the first component of a PCA decomposition on the processed data accounting for more than 99% of the total variance ratio, thus implying only minor modifications of the average structure across the probed surface. The spectrum exhibits two broad features around 590 cm^{-1} and 1090 cm^{-1}, the latter including a weaker, well-defined peak at 950 cm^{-1}. These observations are consistent with literature data on sodium- and calcium-containing silicates and aluminosilicates.[8,16–22] At low wavenumbers (200-700 cm^{-1}), the Raman signal mostly originates from Si-O-Si bending vibrations, providing information on bond angles and network connectivity. The bands at ∼590 and ∼490 cm^{-1} are typically associated to the breathing modes of 3- and 4-member tetrahedra rings observed in vitreous silica, also referred to as the D_2 and D_1 bands.[21–25] In the 850-1250 cm^{-1} range, the high-wavenumber envelope arises from the convoluted signals of T-O (T = Si, Al) stretching vibrations involving Q^n tetrahedral units (Q^n is a TO_4 tetrahedron sharing n bridging oxygens with other tetrahedra) and contains information on the local structure of the aluminosilicate network. Specifically, the contributions at 950 and 1090 cm^{-1} observed here are reported to mainly originate from Q^2 and Q^3 structural units, respectively.[16,18,26] Average spectra of the other glass samples exhibit the same features, with composition-induced variations as the proportion of network formers (Si, Al) and modifiers (Ca, Na) changes. This comparison is provided in Fig. S1 (Supporting Information).

In Fig. 4, we illustrate the dataset quality by comparing Raman spectra recorded across the analyzed surface at fixed X position. Apart from rare

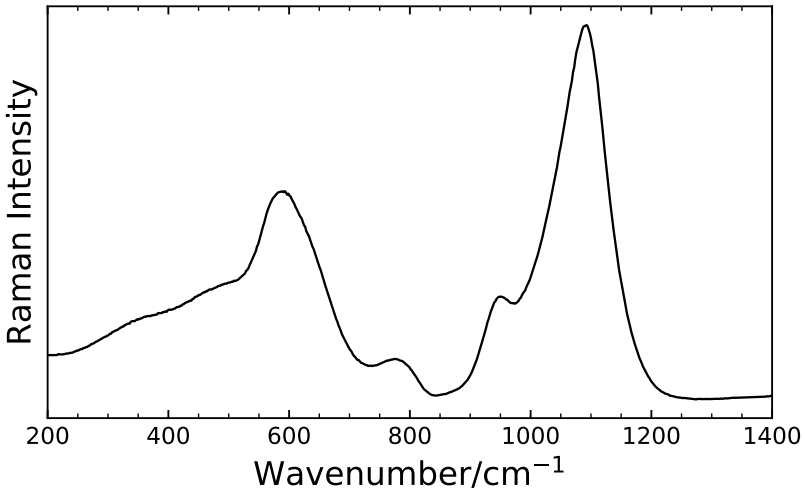

Figure 3: Average Raman response of glass sample C_0.

instances of background variations due to fluorescence or surface pollution, only minor fluctuations are observed and one may argue that they all fall within experimental noise. Yet in some very localized events involving no more than a few neighbour spectra, we observe a small broadening of the 590 cm^{-1} band toward high wavenumbers, as well as fluctuations of the intensity of the Q^2 band at 950 cm^{-1}. Modifications of the broad 1090 cm^{-1} band are not easily identifiable from this simple spectra comparison, limiting further analysis.

Raman images were reconstructed by simply using Raman intensities at different wavenumbers. Although this parameter should be interpreted with care when applied to the broad Raman response of amorphous materials, it presents the advantage of quickly providing information on the most affected vibrations without the need for additional processing. By scanning through the Raman intensity images across the spectral range, we uncovered a beautiful macroscopic wavy pattern, represented in Fig. 5(a) using the Raman intensity at 950 cm^{-1} (I_{950}). This pattern is distinguishable on most of the spectral range, although presenting significant variations in image noise and contrast depending on the chosen wavenumber. Surprisingly, the most resolved images are obtained in the vicinity of the 950 cm^{-1} and 590 cm^{-1} features. Around the latter, we observe that Raman intensity images below and above 590 cm^{-1} are complementary to each other, and thus that the Raman spectral weight shifts from below to above 590 cm^{-1} (the reader may refer to Fig. S2 (Supplementary Information) to observe this particuliar behavior). A comparison of Raman spectra from contrasted areas of the image

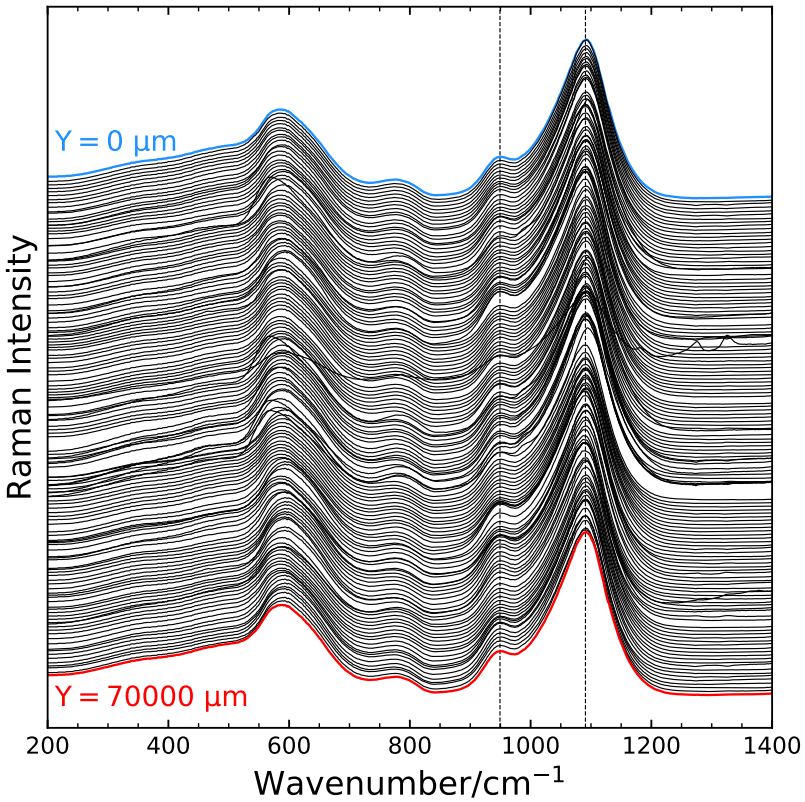

Figure 4: Comparison of all 141 processed Raman acquisitions across the sample at position X=35000 µm. The spectra are shifted vertically for clarity (note that successive spectra were recorded 500 µm apart from each other). Rare inconsistencies in vertical shift arise from residual background variations. Dashed lines indicate the 950 and 1090 cm^{-1} bands as guides to the eye.

is provided in Fig. 5(b).

Despite a spatial step of 500 µm, the macroscopic pattern in Fig. 5(a) is remarkably detailed. It is characterized by singular wavy features that we shall describe as overlapping layers spreading outwards from the center of the image. These features become narrower near the center of the glass sample, where the melt was poured, and strikingly remind of what is occurring during the casting process, that is, the spreading of the viscous melt from the casting area. To illustrate this comparison, we recorded the casting of a sample silicate melt using an Infrared (IR) camera. Fig. 6 shows a selection of images from the recording that were taken at key moments of the casting process. Looking at Fig. 6(a) and 6(b), it is clear that the temperature gradient at the surface of the casted sample exhibits a pattern that is very similar to that of the Raman image. In fact, all samples exhibit similar patterns at their surface, resulting in a range of figures evocative of the casting process (Fig. S3 (Supporting Information)).

The Raman image exhibits well-resolved boundaries between contrasted areas, indicating sharp changes in Raman response. The fluctuations appearing as noise in Fig. 4 are then obviously spatially correlated in Fig. 5(a). It is also worth noting that Fig. 5(a) does not appear to be correlated at all with the sample topography (Fig. 2). The I_{950} parameter varies by up to ∼20% across the surface of the sample; it is most intense on the left side of the image, and the lowest intensities are obtained in the folded layers described earlier. Considering the timeline of the casting process, we believe that areas exhibiting the highest I_{950} values likely consist of glass from the early stage of the casting (Fig. 6(a)). Subsequently, the large wavy patterns represented by lower I_{950} values appear to be more representative of the material that was poured toward the end of the process (Fig. 6(b)). As I_{950} increases, the broad 1090 cm^{-1} band slightly shifts to lower wavenumbers (Fig. 5(b)), implying a decrease of the population of the more polymerized Q^n units. In addition, the 590 cm^{-1} band shifts toward high wavenumbers. This shift was anticipated from the Raman images around this feature, and indicates changes in inter-tetrahedral Si-O-Si bond angles distribution and ring statistics. We probed the position of the low-wavenumber band by following the center of mass of the 200-730 cm^{-1} envelope, introducing Raman parameter σ described by Deschamps *et al.*[27] This parameter accounts for variations of network connectivity occuring upon changes in the medium-range order. It was used as an indicator of the densification ratio of vitreous silica at room temperature,[27] and more recently for local mapping of fictive temperature variations in fused silica.[28] In Fig. 7, the representation of this parameter indicates that σ increases by ∼10 cm^{-1} across the surface of the sample. The map exhibits the same well-resolved pattern as the intensity at

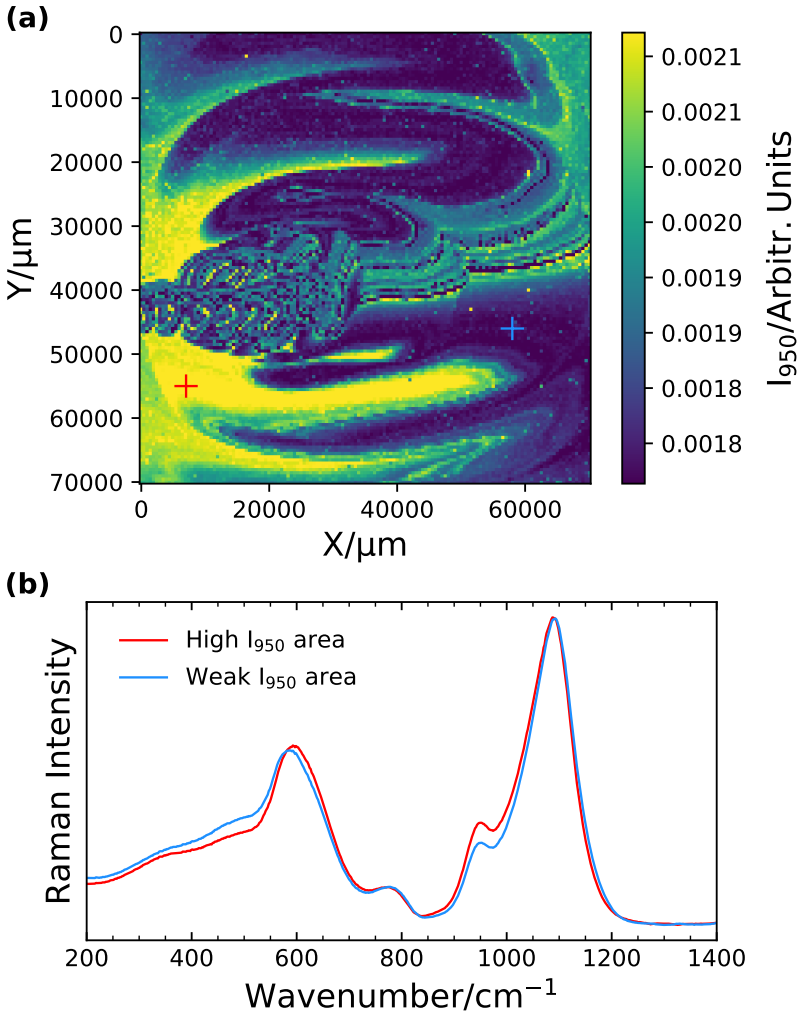

Figure 5: (a) Raman image of the sample surface, reconstructed using the intensity of the band at 950 cm^{-1} (I_{950}). (b) Normalized Raman spectra from areas of high and weak I_{950}. The spectra positions are indicated on the image by markers of same colors.

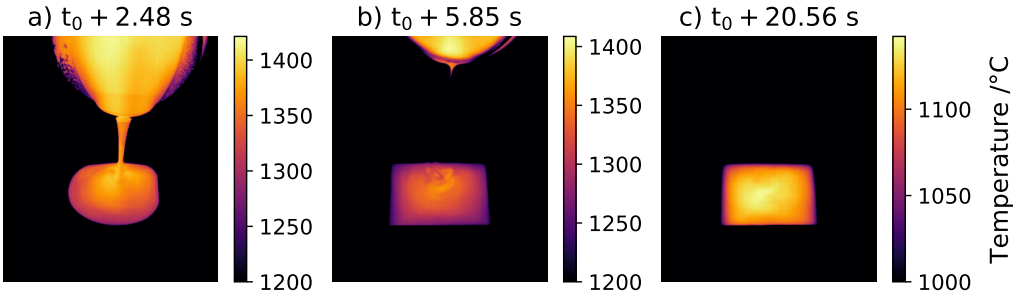

Figure 6: Infrared (IR) images of the casting of a silicate melt (Optris PI G7 640 Infrared Camera / λ =7.9 µm), with t_0 the beginning of the casting process. Colorbars may be interpreted qualitatively, the process temperature being too close to the camera upper limit of 1500°C. a) Early stage of the casting process; the melt is poured over the metallic suface. b) End of the casting process; the crucible is pulled away from the casting area, leaving a thin stream of melt in its path. c) Casted glass sample after ∼15 s of air-quenching.

950 cm^{-1}, which emphasizes the strong correlation between the increase of both parameters and the casting process.

Discussion

Spatial reconstructions of the sample surface from Raman parameters I_{950} and σ evidence a correlation that materializes in the form of a macroscopic pattern evocative of the glass casting process. Specifically, the early stage of the casting process is distinguished by higher Raman intensities at 950 cm^{-1} and the shift of the broad 200-730 cm^{-1} feature toward higher wavenumbers. It is known that changes in Raman response of the Si-O bending envelope and the vibrational modes of Q^n structural units may arise from local composition, structure or stress state fluctuations. Indeed, the bending and stretching massifs are strongly correlated, and it has been documented that the joint modifications of these envelopes may be used to identify variations in chemistry and processing temperature, for example.[29,30]

It is obvious from the IR recordings that the Raman observables find some meaning in the sample thermal history. As soon as the melt begins to be casted, differences in quench rates will generate temperature gradients within the glass sample, as illustrated in Fig. 6(a). Naturally, higher cooling rates are obtained when the 1550°C melt is rapidly cooled on the metallic surface. Follows a decrease of the cooling rate over time, resulting in a temperature gradient at the surface of the sample (Fig. 6(b)) that will

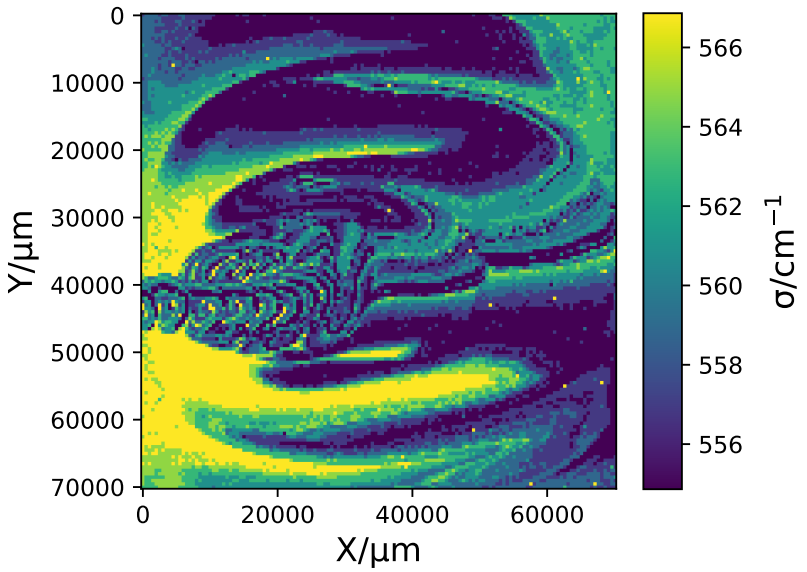

Figure 7: Evolution of Raman parameter σ, center of mass of the 200-730 cm^{-1} envelope, across the surface of the sample.

eventually homogenize upon further cooling (Fig. 6(c)) and subsequent annealing. From a structural standpoint, the increase of the intensity of the Q^2 Si-O stretching mode in areas associated with the early stage of the casting process is consistent with a greater disorder of the Q^n entities and depolymerization of the silicate network in the high temperature melt. This result is in agreement with ^{29}Si NMR and Raman investigations of the influence of fictive temperature in different silicate systems.[19,31–33] Additionally, σ values were also reported to increase with fictive temperature.[28] From these observations, we infer that our thermal treatment properly relieved thermal stresses but was not sufficiently long to achieve full reorganization of the local structure. These local fluctuations are reflected in the Raman spectra, and Raman images thus reveal the fingerprint of T_f variations at the surface of the glass piece. We did not attempt to correlate our Raman parameters with precise values of fictive temperature as this procedure would require a calibration curve and was thus beyond the scope of this work. It should be noted however that the range of σ values ($\sim$10 cm^{-1}) obtained from our analysis is quite large compared to what was obtained in T_f mapping across ultra-short pulse (USP) laser modified samples.[28] Moreover, it is unlikely that our process achieved comparable cooling rates and thus large T_f fluctuations. These considerations tend to indicate that cooling rate and T_f only partly account for the variations of parameters I_{950} and σ.

Assuming that internal stresses were properly relieved during the annealing procedure, modifications of the Raman spectra may also originate from local composition gradients at the surface of the glass piece. The network connectivity (and thus, Si-O bond angles) and Q^n speciation are intimately linked to composition. Higher proportions of network modifiers will decrease network polymerization, thus shifting the stretching envelope downward. Similarly, increasing proportions of modifiers content have shown to affect the 600 cm^{-1} feature in Na- and Ca-bearing aluminosilicates.[20,34] Because Ca has a tendency to adopt a Q^2 conformation rather than Q^3, we infer that the fluctuations in I_{950} may also be attributed to local variations of Ca (and Si) content at the surface of the glass piece.[35] Considering that the extent of modification of I_{950} at the surface of a sample is smaller than the differences within the sample set, we estimate that these variations are $<$1 wt%. Lack of homogeneity of the melt may originate from insufficient mixing during the process and should be addressed. Unfortunately, chemical mapping was not performed on the samples as very few Energy Dispersive X-ray Spectroscopy (EDX) and X-ray Fluorescence (XRF) apparatus may accommodate such large and heavy (up to 1 kg) samples. A detailed investigation of the composition fluctuations at the surface of similar samples may be the subject of future work regarding this matter. Finally, we ruled out the influence from water content as vibrations from the Si-OH linkages were not detected in the 2840-3750 cm^{-1} range.

Conclusions

Raman imaging was used to probe local fluctuations of Raman response over centimeter-scale areas at the surface of casted glass samples. We observed that modifications of the Raman spectra across the surface of the sample are rather small and localized across the covered spectral range. Thanks to spatial correlation, structural information was extracted from what may be confused with noise by simple spectra comparison. Specifically, the reconstruction of high-quality Raman images evidenced macroscopic patterns of small local variations in Q^n speciation and Si-O-Si bending vibrations across the analyzed surface. The contrasts on the Raman observables show striking resemblance with IR images of the making of the sample, and can therefore identify areas consisting of material from the early and late stage of the manufacturing process. The fluctuations likely originate from two combined effects: 1. Fictive temperature variations, induced by an evolution of the cooling rate over the course of the casting process, 2. Composition gradients within the crucible, probably due to insufficient mixing of the melt.

Structural and chemical changes originating from the manufacturing process are therefore printed at the surface of the glass pieces, and their fingerprint revealed by Raman imaging. We believe that our results should not compromise the overall homogeneity of the samples at their core, but rather highlight the sensitivity of Raman spectroscopy to accurately probe such microscopic inhomogeneities.

This work shows the interest of gathering and processing large datasets to properly assess chemical and structural homogeneity. Raman imaging is therefore particularly suited to the analysis of materials exhibiting a wide distribution of local environments, such as glasses. Large Raman images such as those provided in this paper may find applications in cultural heritage and geosciences, providing new insights on ancient manufacturing processes and geological phenomena.

Acknowledgments

We thank the Glass formulation department of Saint-Gobain Recherche Paris (SGR Paris, Aubervilliers, France) for assistance in the synthesis of the glass samples and N. Raimboux (CEMHTI, CNRS) for her help in the manufacturing of custom sample holders for Raman measurements. This research was conducted under funding from the Agence Nationale de la Recherche (ANR) MAGI project ANR-17-CE08-0019, and from the EquipeX PlaneX ANR-11-EQPX-36.

References

[1] D. R. Neuville, D. de Ligny, G. S. Henderson, *Rev. Mineral. Geochemistry* **2014**; *78*, 509.

[2] B. T. Poe, P. F. McMillan, B. Coté, D. Massiot, J. P. Coutures, *J. Am. Ceram. Soc.* **1994**; *77*, 1832.

[3] B. O. Mysen, J. D. Frantz, *Contrib. to Mineral. Petrol.* **1994**; *117*, 1.

[4] I. Daniel, P. Gillet, B. T. Poe, P. F. McMillan, *Phys. Chem. Miner.* **1995**; *22*, 74.

[5] D. R. Neuville, B. O. Mysen, *Geochim. Cosmochim. Acta* **1996**; *60*, 1727.

[6] M. Dutreilh-Colas, A. Canizares, A. Blin, S. Ory, P. Simon, *J. Am. Ceram. Soc.* **2011**; *94*, 2087.

[7] O. N. Koroleva, V. N. Anfilogov, A. Shatskiy, K. D. Litasov, *J. Non. Cryst. Solids* **2013**; *375*, 62.

[8] T. K. Bechgaard, G. Scannell, L. Huang, R. E. Youngman, J. C. Mauro, M. M. Smedskjaer, *J. Non. Cryst. Solids* **2017**; *470*, 145.

[9] M. Maguregui, U. Knuutinen, J. Trebolazabala, H. Morillas, K. Castro, I. Martinez-Arkarazo, J. M. Madariaga, *Anal. Bioanal. Chem.* **2012**; *402*, 1529.

[10] P. Colomban, M. Havel, *J. Raman Spectrosc.* **2002**; *33*, 789.

[11] O. A. Maslova, G. Guimbretière, M. R. Ammar, L. Desgranges, C. Jégou, A. Canizarès, P. Simon, *Mater. Charact.* **2017**; *129*, 260.

[12] Y. Liu, M. Shimizu, X. Wang, B. Zhu, M. Sakakura, Y. Shimotsuma, J. Qiu, K. Miura, K. Hirao, *Chem. Phys. Lett.* **2009**; *477*, 122.

[13] A. Casanova, A. Gomis-Berenguer, A. Canizares, P. Simon, D. Calzada, C. O. Ania, *Materials (Basel).* **2020**; *13*, 217.

[14] W. Woelffel, C. Claireaux, M. J. Toplis, E. Burov, É. Barthel, A. Shukla, J. Biscaras, M. H. Chopinet, E. Gouillart, *J. Non. Cryst. Solids* **2015**; *428*, 121.

[15] L. Mercury, K. I. Shmulovich, I. Bergonzi, A. Canizarès, P. Simon, *J. Phys. Chem. C* **2016**; *120*, 7697.

[16] S. A. Brawer, W. B. White, *J. Chem. Phys.* **1975**; *63*, 2421.

[17] S. A. Brawer, W. B. White, *J. Non. Cryst. Solids* **1977**; *23*, 261.

[18] T. Furukawa, K. E. Fox, W. B. White, *J. Chem. Phys.* **1981**; *75*, 3226.

[19] C. Levelut, R. Le Parc, A. Faivre, B. Champagnon, *J. Non. Cryst. Solids* **2006**; *352*, 4495.

[20] B. O. Mysen, M. J. Toplis, *Am. Mineral.* **2007**; *92*, 933.

[21] C. Le Losq, D. R. Neuville, *Chem. Geol.* **2013**; *346*, 57.

[22] C. Le Losq, D. R. Neuville, P. Florian, G. S. Henderson, D. Massiot, *Geochim. Cosmochim. Acta* **2014**; *126*, 495.

[23] S. K. Sharma, J. F. Mammone, M. F. Nicol, *Nature* **1981**; *292*, 140.

[24] F. L. Galeener, *J. Non. Cryst. Solids* **1982**; *49*, 53.

[25] F. L. Galeener, *Solid State Commun.* **1982**; *44*, 1037.

[26] P. McMillan, *Am. Mineral.* **1984**; *69*, 622.

[27] T. Deschamps, A. Kassir-Bodon, C. Sonneville, J. Margueritat, C. Martinet, D. de Ligny, A. Mermet, B. Champagnon, *J. Phys. Condens. Matter* **2013**; *25*, 025402.

[28] M. Bergler, K. Cvecek, F. Werr, M. Brehl, D. De Ligny, M. Schmidt, *Int. J. Extrem. Manuf.* **2020**; *2*, 035001.

[29] P. Colomban, O. Paulsen, *J. Am. Ceram. Soc.* **2005**; *88*, 390.

[30] P. Colomban, A. Tournie, L. Bellot-Gurlet, *J. Raman Spectrosc.* **2006**; *37*, 841.

[31] M. E. Brandriss, J. F. Stebbins, *Geochim. Cosmochim. Acta* **1988**; *52*, 2659.

[32] W. J. Malfait, W. E. Halter, *Phys. Rev. B - Condens. Matter Mater. Phys.* **2008**; *77*, 1.

[33] J. Tan, S. Zhao, W. Wang, G. Davies, X. Mo, *Mater. Sci. Eng. B Solid-State Mater. Adv. Technol.* **2004**; *106*, 295.

[34] D. R. Neuville, L. Cormier, D. Massiot, *Chem. Geol.* **2006**; *229*, 173.

[35] A. R. Jones, R. Winter, G. N. Greaves, I. H. Smith, *J. Non. Cryst. Solids* **2001**; *293-295*, 87.